# Numerical Investigation to the Effect of Initial Guess for Phase-Field Models

Sungha Yoon[1], Jian Wang[2], Chaeyoung Lee[1], Junxiang Yang[1],
Jintae Park[1], Hyundong Kim[1] and Junseok Kim[1,*]

[1]*Department of Mathematics, Korea University, Seoul 02841, Republic of Korea.*
[2]*School of Mathematics and Statistics, Nanjing University of Information Science
and Technology, Nanjing 210044, China.*

**Abstract.** The construction of relevant initial conditions in the phase-field models for interfacial problems is discussed. If the model is supposed to have a local equilibrium at the interface, it must be based on a local distance function. However, since for the Cartesian coordinates non-uniform boundaries occur, the initial conditions have to be corrected in order to match the actual phenomena. We discuss the volume correction method, image initialisation, non-overlapping multi component concentration, etc. The methods presented can be used in the initial guess constructions for various phase-field models.

**AMS subject classifications**: 65M06, 68U10

**Key words**: Allen-Cahn equation, Cahn-Hilliard equation, phase-field model, level set function.

## 1. Introduction

The phase-field model, a mathematical model for solving interfacial problems, was introduced in [24, 39]. Examples of such problems include dendritic growth [34, 58], spinodal decomposition [45], micro-phase pattern formation [11, 61], image inpainting [5], image segmentation [55], vesicle dynamics [47, 53], tumor growth [13, 44], two-phase flow [1, 38], and multi-phase fluid flow [3, 23, 59]. In the phase-field model, the boundary conditions at the interface are replaced by the phase-field equation. The phase-field function takes distinct values at each phase and has a smooth interfacial transition layer between distinct values. We define the interface as a contour in the two-dimensional space or an isosurface in the three-dimensional space. In the limit of an infinitesimal interfacial parameter, we can have the correct interfacial dynamics. Therefore, instead of direct treatment of the corresponding boundary conditions at the interface, the interfacial related problems can be reduced to the solution of equations over the whole domain.

---

The first example of the phase-field equations is the Allen-Cahn (AC) equation [2] which governs the motion of anti-phase boundaries in crystalline solids

$$\frac{\partial \phi}{\partial t}(\mathbf{x}, t) = -\frac{F'(\phi(\mathbf{x}, t))}{\epsilon^2} + \Delta \phi(\mathbf{x}, t), \quad \mathbf{x} \in \Omega, \quad t > 0, \tag{1.1}$$

where $\Omega$ is a domain, $\phi$ the difference of concentrations, $F(\phi) = 0.25(\phi^2 - 1)^2$, and $\epsilon$ a positive parameter related to the interfacial thickness. Fig. 1 shows the temporal evolution of the contour and the isosurface of the numerical solutions of the AC equation (1.1) with the initial conditions described in [42].

Next example is the dendritic growth equations with a four-fold symmetry in the two-dimensional space [34, 58]

$$\epsilon^2(\phi)\frac{\partial \phi}{\partial t} = \nabla \cdot \left(\epsilon^2(\phi)\nabla\phi\right) + \left[\phi - \lambda U\left(1 - \phi^2\right)\right]\left(1 - \phi^2\right)$$
$$+ \left(|\nabla\phi|^2 \epsilon(\phi)\frac{\partial \epsilon(\phi)}{\partial \phi_x}\right)_x + \left(|\nabla\phi|^2 \epsilon(\phi)\frac{\partial \epsilon(\phi)}{\partial \phi_y}\right)_y,$$
$$\frac{\partial U}{\partial t} = D\Delta U + \frac{1}{2}\frac{\partial \phi}{\partial t}, \quad \text{for} \quad \mathbf{x} \in \Omega, \quad t > 0, \tag{1.2}$$
$$\epsilon(\phi) = W_0\left(1 - 3\delta_4 + 4\delta_4 \frac{\phi_x^4 + \phi_y^4}{|\nabla\phi|^4}\right),$$

where $\Omega$ is a domain, $\phi(\mathbf{x}, t)$ the order parameter taking values between $-1$ (liquid phase) and 1 (solid phase), $W_0$ the measure of the interface width, $\epsilon(\phi)$ the anisotropic function, $\delta_4$ the anisotropic strength, $\lambda$ the dimensionless coupling parameter, $D$ the diffusion rate
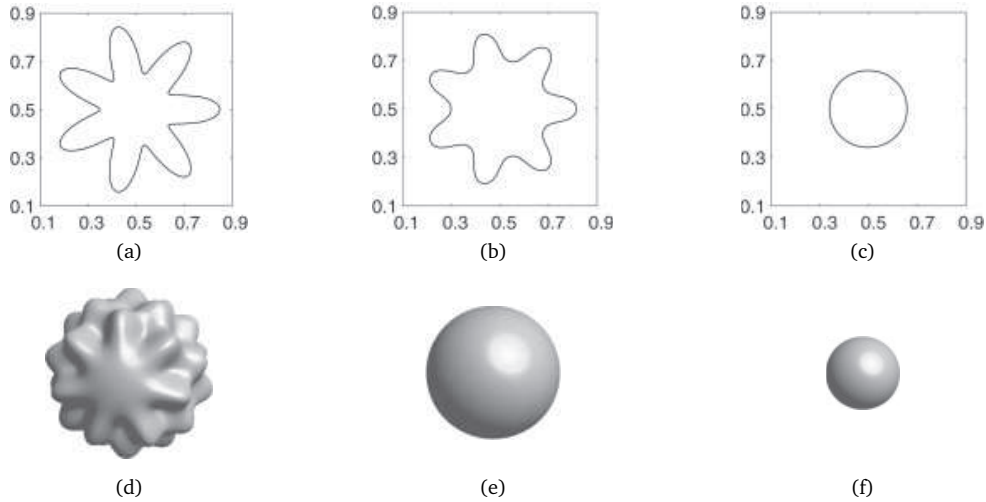


Figure 1: Motion by mean curvature. (a)-(c) and (d)-(f) show the results in two- and three-dimensional spaces, respectively. Reprinted from Li *et al.* [42] with permission of Elsevier Science.
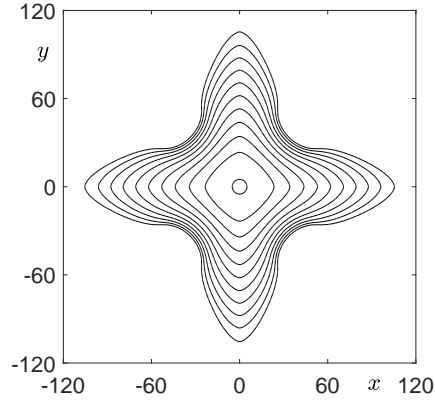
Figure 2: Temporal evolution of dendritic growth (1.2) with four-fold symmetry in 2D. Reprinted from Jeong and Kim [34] with permission from Elsevier Science.

of the temperature and $U(\mathbf{x}, t)$ the dimensionless temperature field. Fig. 2 illustrates the temporal evolution of dendritic growth (1.2) in two-dimensional space.

The three-dimensional dendritic growth model is

$$
\epsilon^2(\phi)\frac{\partial \phi}{\partial t} = \nabla \cdot \left( \epsilon^2(\phi)\nabla \phi \right) + \left[ \phi - \lambda U \left( 1 - \phi^2 \right) \right]\left( 1 - \phi^2 \right)
$$
$$
+ \left( |\nabla \phi|^2 \epsilon(\phi)\frac{\partial \epsilon(\phi)}{\partial \phi_x} \right)_x + \left( |\nabla \phi|^2 \epsilon(\phi)\frac{\partial \epsilon(\phi)}{\partial \phi_y} \right)_y + \left( |\nabla \phi|^2 \epsilon(\phi)\frac{\partial \epsilon(\phi)}{\partial \phi_z} \right)_z,
$$
$$
\frac{\partial U}{\partial t} = D\Delta U + \frac{1}{2}\frac{\partial \phi}{\partial t}, \tag{1.3}
$$
$$
\epsilon(\phi) = W_0 \left( 1 - 3\delta_4 + 4\delta_4\frac{\phi_x^4 + \phi_y^4 + \phi_z^4}{|\nabla \phi|^4} \right).
$$

Fig. 3 illustrates the temporal evolution of dendritic growth (1.3) in three-dimensional space.

Another representative example of the phase-field model is the Cahn-Hilliard (CH)
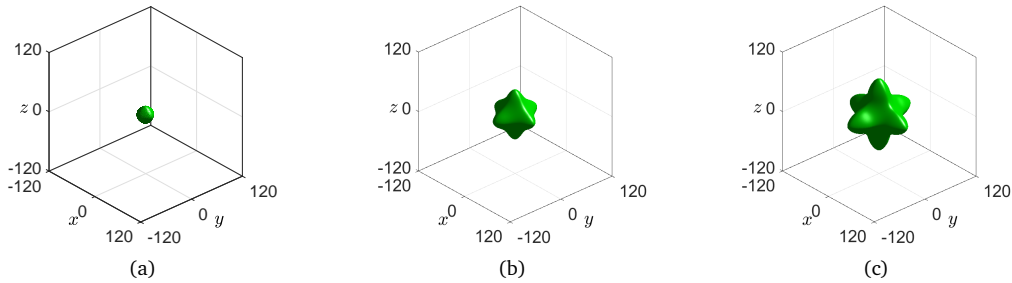


Figure 3: Temporal evolution of dendritic growth (1.3) in 3D. Reprinted from Jeong and Kim [34] with permission of Elsevier Science.

equation [7, 8]

$$\frac{\partial \phi(\mathbf{x}, t)}{\partial t} = \Delta \mu(\mathbf{x}, t), \quad \mathbf{x} \in \Omega, \quad t > 0,$$

$$\mu(\mathbf{x}, t) = F'\big(\phi(\mathbf{x}, t)\big) - \epsilon^2 \Delta \phi(\mathbf{x}, t),$$

(1.4)

where $\Omega \subset \mathbb{R}^d$, $d = 1, 2, 3$ is a domain, $F(\phi) = 0.25(\phi^2 - 1)^2$ the double well potential energy, and $\epsilon$ a positive parameter. The phase field $\phi(\mathbf{x}, t)$ which ranges between $-1$ and $1$ is defined as the difference between the mole fractions of binary mixtures. As a typical example of the phase-field model, the CH equation has been widely studied in various fields of scientific research. Since AC and CH equations are closely connected, various related studies have been conducted [12, 43, 46]. The CH equation (1.4) with random initial condition is widely used to simulate the spinodal decomposition. Figs. 4(a)-4(c) and 4(d)-4(f) show the evolutions of binary and multi-component spinodal decomposition [51, 56], respectively.

Furthermore, the CH equation with the specific initial condition

$$\phi(\mathbf{x}, 0) = 2(x - 0.5)$$

(1.5)

can be used to simulate the spinodal decomposition and the nucleation taking place simultaneously. Figs. 5(a)-5(d) show the temporal evolutions of the spinodal decomposition and the nucleation in the unit domain [28] with the initial condition (1.5).

Many important problems in materials science and thin film technologies are related to open curve/surface evolution problems. One such topic is the solid-state dewetting phenomenon [19, 31, 35, 36]. It arises in various systems and is associated with the category
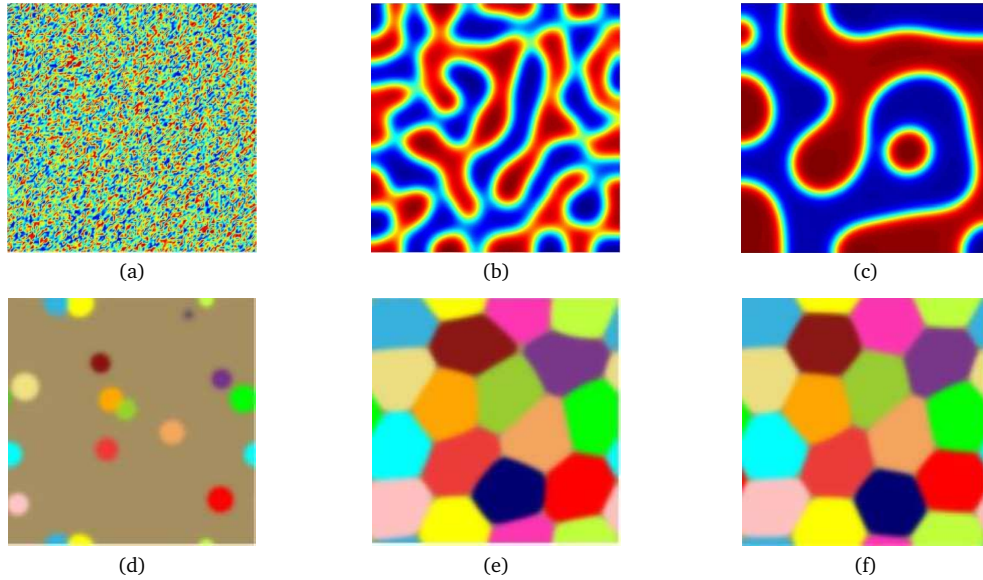


Figure 4: Temporal evolution of spinodal decomposition. (a)-(c) and (d)-(f) show the results for binary and multi-component spinodal decomposition, respectively. Adapted from [56] and [51] with permission of Elsevier Science.
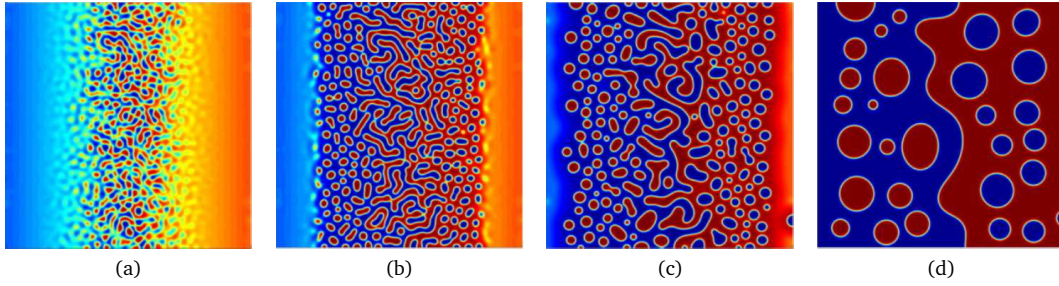
Figure 5: Temporal evolutions of spinodal decomposition and nucleation. Adapted from [28] with permission of Elsevier Science.

of capillarity-controlled interface or surface evolutions. The dewetting process is mathematically modeled and studied by the sharp-interface method or the phase-field method. A schematic evolution process of the solid-state dewetting of a thin film on a substrate is presented in Fig. 6. The initial state is shown in Fig. 6(a), the intermediate state in Fig. 6(b), and the final profile of pinch-off state in Fig. 6(c). The evolution is modelled by the CH equation.

Next, there is the following governing equations of diblock copolymer [11]:

$$\frac{\partial \phi(\mathbf{x}, t)}{\partial t} = \Delta \mu(\mathbf{x}, t) - \alpha\big(\phi(\mathbf{x}, t) - \bar{\phi}(\mathbf{x}, t)\big), \tag{1.6}$$

$$\mu(\mathbf{x}, t) = F'\big(\phi(\mathbf{x}, t)\big) - \epsilon^2 \Delta \phi(\mathbf{x}, t), \tag{1.7}$$

where

$$\bar{\phi}(\mathbf{x}, t) = \frac{1}{\Omega} \int_{\Omega} \phi(\mathbf{x}, t) d\mathbf{x}.$$

Figs. 7(a) and 7(b) show the snapshots of the diblock copolymer (1.7) simulations with random initial conditions around $\bar{\phi} = 0$ and $\bar{\phi} = 0.3$, respectively.

The Swift-Hohenberg (SH) equation

$$\frac{\partial \phi(\mathbf{x}, t)}{\partial t} = \epsilon \phi(\mathbf{x}, t) - (\Delta + 1)^2 \phi(\mathbf{x}, t) + g \phi^2(\mathbf{x}, t) - \phi^3(\mathbf{x}, t), \quad \mathbf{x} \in \Omega, \quad t > 0 \tag{1.8}$$

with periodic boundary condition and random initial condition [49] is used in cellular materials, crystallography, metallurgy [26]. Fig. 8 shows two snapshots of numerical solutions with random initial conditions. The phase-field model with random initial conditions are often used since the results of shape over time by solving the differential equation (1.8) are
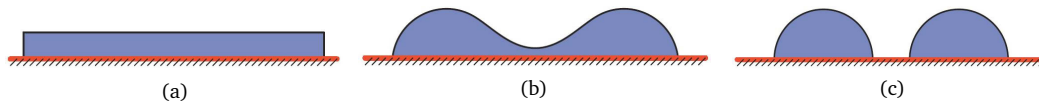


Figure 6: The solid-state dewetting of a thin film on a substrate. Reprinted from Jiang *et al.* [35] with permission of Elsevier Science.
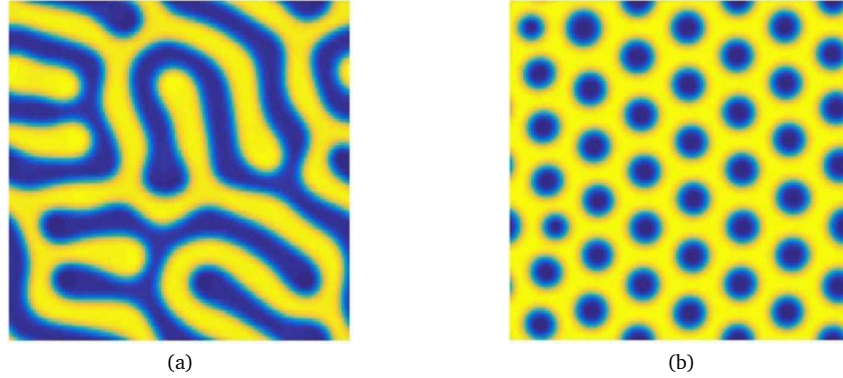
Figure 7: (a) and (b) are the snapshots of the results of diblock copolymer (1.7) simulation with random initial condition around $\bar{\phi} = 0$ and $\bar{\phi} = 0.3$, respectively. Adapted from [11] with permission of Elsevier Science.

qualitatively similar to each other for identical model parameters. Fig. 8 depicts the snapshots of solutions of the SH equation (1.8) with random initial conditions and different model parameters. Furthermore, the modified phase-field crystal equation

$$\frac{\partial \phi(\mathbf{x}, t)}{\partial t} = \Delta \left[ \phi^3(\mathbf{x}, t) + (1 - \epsilon)\phi(\mathbf{x}, t) + 2\Delta\phi(\mathbf{x}, t) + \Delta^2\phi(\mathbf{x}, t) \right], \qquad (1.9)$$

introduced in [48] finds applications in isotropic phase separation and crystallisation of undercooled liquid-liquid interface. There are several theoretical papers concerning this topic [20, 21] and the related numerical methods, including the operator splitting method [52], convex splitting method [29], and spectral method [17]. Fig. 9 shows the evolution of phase field crystal equation (1.9) with a randomly distributed initial values in the two- and three-dimensional spaces.

In computational fluid dynamics, the Cahn-Hilliard-Navier-Stokes (CHNS) model is used to model various two-phase flow phenomena [30]. The most typical benchmark prob-
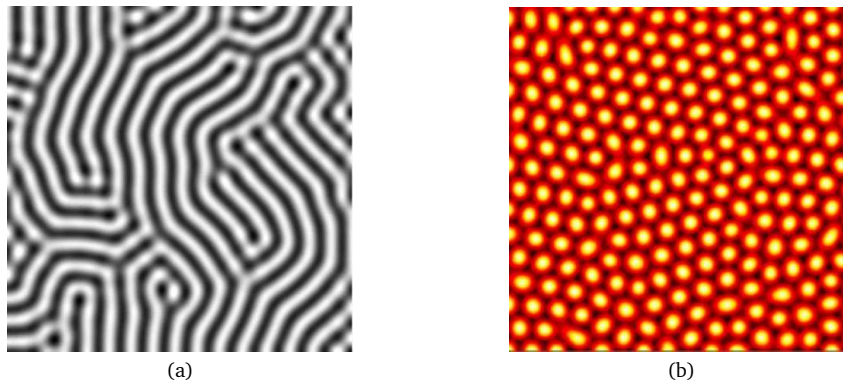


Figure 8: Snapshots of the numerical solutions of the SH equation (1.8) with random initial conditions. Reprinted from [16] with permission of Elsevier Science.
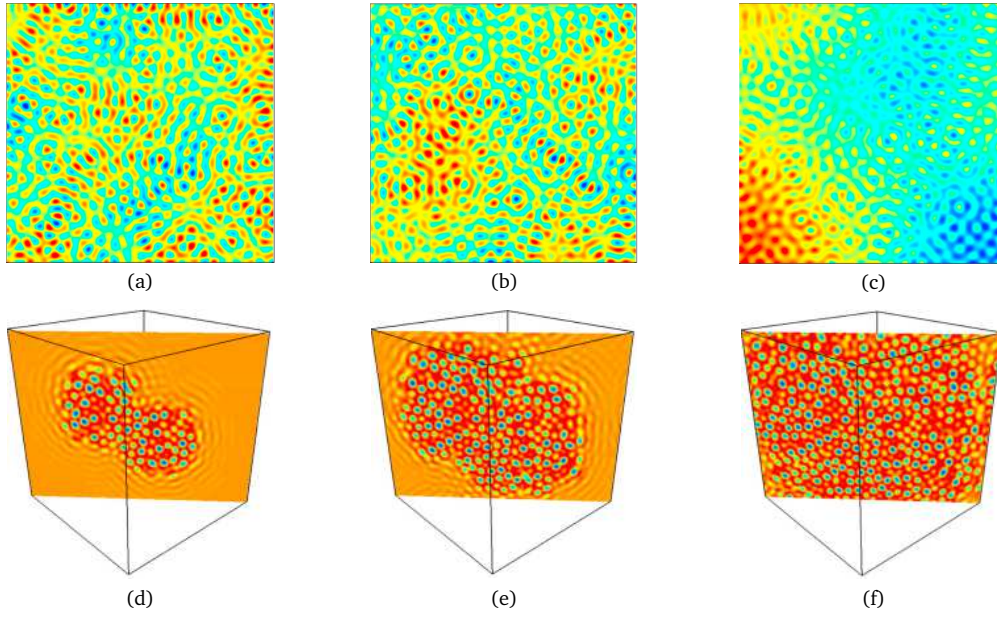
Figure 9: Temporal evolution of phase field crystal equation (1.9). (a)-(c): two-dimensional space. (d)-(f): three-dimensional space in slice view. Reprinted from [16, 48] with permissions of Elsevier Science.

lem for the CHNS model with variable density is the Rayleigh-Taylor (RT) instability. We can take the initial condition of the CH equation as a cosine function with a small amplitude, then the interfacial instability evolves with time to form the RT instability. Fig. 10 shows the temporal evolution of the RT instability [50].

Various analytic and experimental studies on the deformation of biological vesicle membranes use the phase-field approach [47, 53]. The governing equation derived from the elastic bending energy is

$$\frac{\partial \phi}{\partial t}(\mathbf{x}, t) = -g\big(\phi(\mathbf{x}, t)\big) - 2M\big(B(\phi(\mathbf{x}, t)) - \beta\big)f\big(\phi(\mathbf{x}, t)\big) + \gamma(t)F\big(\phi(\mathbf{x}, t)\big),$$

where $M$ is a large penalty constant, $g(\phi) = \delta W(\phi)/\delta\phi$, and $f(\phi) = \delta B(\phi)/\delta\phi$. Here, $W(\phi)$ is the bending surface energy and $B(\phi)$ the surface area. For the volume constraints, one uses the space-time dependent Lagrange multiplier $\gamma(t)F(\phi)$ with $F(\phi)$ and $\gamma(t)$ defined by

$$F(\phi) = \frac{\big(\phi^2 - 1\big)^2}{4} = \frac{\epsilon^2}{2}|\nabla\phi|^2,$$

$$\gamma(t) = \frac{\int_\Omega \big[g(\phi) + 2M(B(\phi) - \beta)f(\phi)\big]\mathrm{d}\mathbf{x}}{\int_\Omega F(\phi)\mathrm{d}\mathbf{x}}.$$

Fig. 11 illustrates the temporal evolution of the vesicle membrane in three-dimensional space.
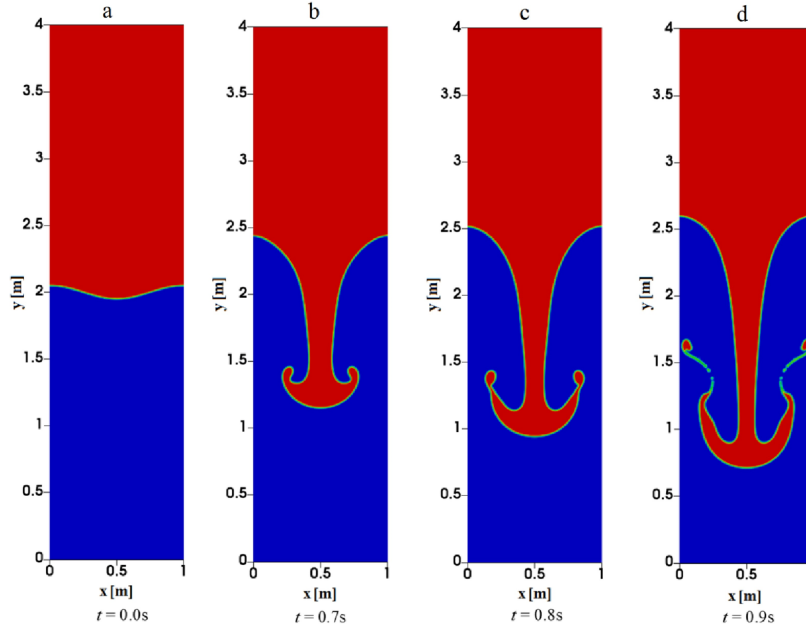
Figure 10: Temporal evolution of the RT instability. Adapted from [50] with permission of Elsevier Science.



Figure 11: Temporal evolution of the vesicle membrane in 3D. Reprinted from Shin *et al.* [47] with permission of Wiley.

The main aim of the present work is to outline constructive initial guesses for the phase-field equations. Since many researchers have difficulties with the appropriate setting of the initial state in experiments, we gather and explain various initial conditions. We discuss the algorithms based on the level set approach with signed distance field [6, 9], which make the initial guess for the phase-field models more suitable and correct.

This paper is organised as follows. Various initial conditions are described in Section 2 and conclusions are made in Section 3.

## 2. Various Initial Conditions

Various initial conditions introduced below are often used in works dealing with the phase-field models treated by finite difference methods. Let us first discretise the two-dimensional domain $\Omega = (a, b) \times (c, d)$. Choose positive integers $N_x$ and $N_y$ such that $h = (b-a)/N_x = (d-c)/N_y$ and consider the corresponding uniform mesh with the set of

cell-centers

$$\Omega_h = \big\{ (x_i, y_j) : x_i = a + (i - 0.5)h, \ y_j = c + (j - 0.5)h, \ 1 \le i \le N_x, \ 1 \le j \le N_y \big\}.$$

Moreover, let $t^n = n\Delta t$ be the discrete time with the time step $\Delta t$ and $\phi_{ij}^n$ a numerical approximation of $\phi(x_i, y_j, t^n)$. The three-dimensional case is a simple extension of the two-dimensional one. The phase-field $\phi$ has values from $-0.9$ to $0.9$ across interfacial transition layer over $2\sqrt{2}\epsilon \tanh^{-1}(0.9)$ length [32]. Hence, if we let $2\sqrt{2}\epsilon \tanh^{-1}(0.9) = hm$, then the interfacial length parameter $\epsilon = \epsilon_m = hm / [2\sqrt{2} \tanh^{-1}(0.9)]$. Here, $\epsilon_m$ means that we have nearly $mh$ transition layer width and is used for our all experiments.

## 2.1. Random initial condition

We take the initial state as $\phi_{ij}^0 = \phi_{ave} + A \operatorname{rand}(x, y)$, where $\phi_{ave}$ is average concentration, $A$ the amplitude of the perturbation and $\operatorname{rand}(x, y)$ uniformly distributed random numbers between $-1$ and $1$. In other words, random initial conditions $\phi_{ij}^0$ for the phase-field model are given as random numbers located between $-1$ and $1$. While using random initial conditions, we can show how well the phase model like the CH equation applies. Fig. 12 shows a random initial condition for $\phi_{ave} = 0$ with $A = 0.1$ on the computational domain $\Omega = (0, 1) \times (0, 1)$.
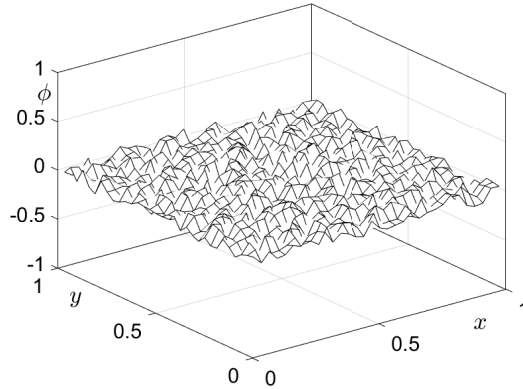


Figure 12: Random initial condition with $\phi_{ave} = 0$ and $A = 0.1$.

## 2.2. Initial conditions for a convergence test

To show the temporal accuracy, the authors of [62] considered the following initial condition

$$\phi(x, y, 0) = 0.05 \sin x \sin y$$

on $\Omega = (0, 2\pi) \times (0, 2\pi)$, Fig. 13(a). They determined a reference numerical solution at a certain time with $\Delta t = 10^{-4}$, $\epsilon = 0.1$ on $400 \times 400$ mesh. Another initial condition — viz.
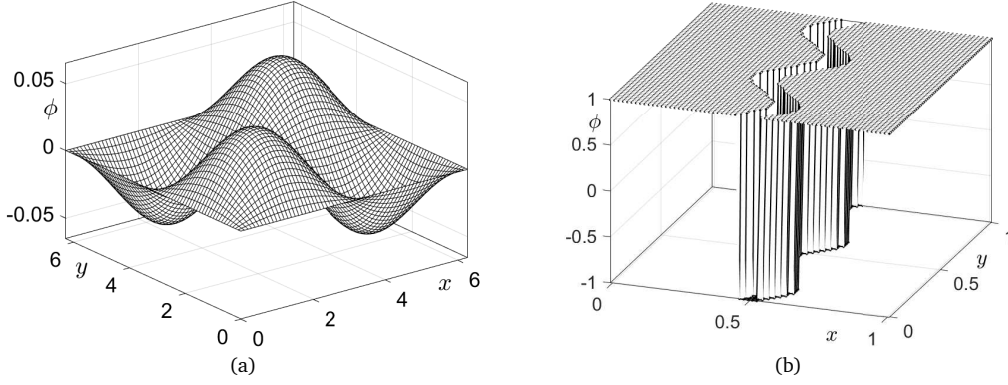
Figure 13: (a) $\phi(x, y, 0) = 0.05 \sin x \sin y$. (b) Mesh plot of the initial condition given by Eq. (2.1).

$$\phi(x, y, 0) = \begin{cases} 1, & \text{if } x > \dfrac{1}{12.8} \sin(4\pi y) + 0.5 + 0.045, \\[2mm] 1, & \text{if } x < \dfrac{1}{12.8} \sin(4\pi y) + 0.5 - 0.045, \\[2mm] -1, & \text{otherwise} \end{cases} \tag{2.1}$$

was used in [25] for numerical convergence tests on $\Omega = (0, 1) \times (0, 1)$, cf. Fig. 13(b).

## 2.3. Rounded rectangle

Considering a the two-phase flow test problem — viz. 2D dam break problem, the authors of [37] used the initial condition

$$\phi(x, y, 0) = \begin{cases} \tanh\left(\dfrac{b - y}{\sqrt{2}\epsilon}\right), & \text{for } x \leq a - r, \quad y \geq b - r, \\[3mm] \tanh\left(\dfrac{a - x}{\sqrt{2}\epsilon}\right), & \text{for } x > a - r, \quad y < b - r, \\[3mm] \tanh\left(\dfrac{r - \sqrt{(x - a + r))^2 + (y - b + r))^2}}{\sqrt{2}\epsilon}\right), & \text{for } x > a - r, \quad y > b - r, \\[3mm] -1, & \text{otherwise.} \end{cases} \tag{2.2}$$

The parameters $a = 0.3$, $b = 0.5$, and $r = 0.04$ are the width, the height, and the radius of the curve of the rounded rectangle, respectively. Fig. 14 shows the initial condition for the uniform mesh size $h = 1/64$ and $\epsilon = \epsilon_2$ on the computational domain $\Omega = (0, 1) \times (0, 1)$.

## 2.4. Initial conditions from a signed distance function

In this section, we discuss how to derive initial conditions from a signed distance function.
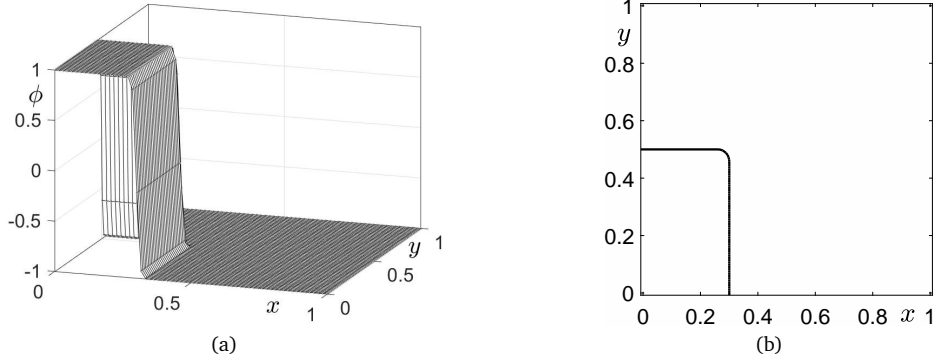
Figure 14: Rectangle with a rounded corner: (a) mesh plot of the phase-field $\phi(x, y, 0)$ and (b) the contour plot of $\phi(x, y, 0)$ at the zero level.

### 2.4.1. Circle and ellipse

Consider the ellipse

$$\frac{x^2}{a^2} + \frac{y^2}{b^2} = 1 \tag{2.3}$$

with the semi-major axis $a$ and semi-minor axis $b$. For $a = b = r$, this is the circle of radius $r$.

Circles and ellipses are used as the initial conditions for simulations of CH and AC equations [10, 15, 60]. We set the initial condition of circle in the domain $\Omega = (-1.2, 1.2) \times (-1.2, 1.2)$ as follows:

$$\phi(x, y, 0) = \tanh\left(\frac{r - \sqrt{x^2 + y^2}}{\sqrt{2}\epsilon}\right). \tag{2.4}$$

Fig. 15 shows the contour plot of the Eq. (2.4) at values $-0.9, 0$ and $0.9$ for $a = b = 1$, $h = 2.4/128$, $\epsilon = \epsilon_8$, and the mesh grid $128 \times 128$ is used.
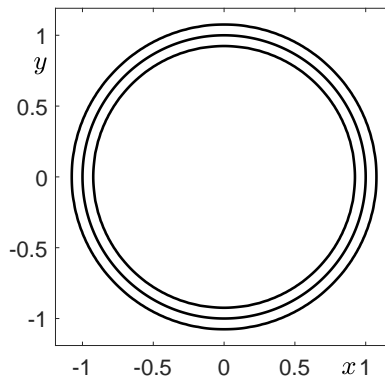


Figure 15: Contour plot of Eq. (2.4) at values $-0.9, 0$, and $0.9$.

To be consistent with the Eq. (2.4), for the general elliptical shape, we may consider the following form:

$$\phi(x,y,0) = \tanh\left(\frac{\sqrt{ab} - \sqrt{bx^2/a + ay^2/b}}{\sqrt{2}\epsilon}\right), \quad a = 2, \quad b = 0.5 \qquad (2.5)$$

in the domain $\Omega = (-2.4, 2.4) \times (-2.4, 2.4)$ with the mesh grid $256 \times 256$ and the other parameters as above. Fig. 16(a) shows the contour of the Eq. (2.5) at the levels $\phi = -0.9, 0, 0.9$. By simple calculations, we can derive the maximum and minimum of the transition width from $\phi = -0.9$ to $\phi = 0.9$ as $\sqrt{8a/b}\epsilon \tanh^{-1}(0.9)$ and $\sqrt{8b/a}\epsilon \tanh^{-1}(0.9)$, respectively. Fig. 16(b) shows the maximum and the minimum of the transition width against $a$ for $b = 0.5$. Here, we scaled the maximum and the minimum values by the transition width of the circular shape — i.e. $\sqrt{8}\epsilon \tanh^{-1}(0.9)$.

Nevertheless, such interfacial profiles do not match actual phenomena, especially in fluid dynamics combined with the phase-field model. The reason for that is because it assumes an equilibrium state in computing variables such as surface tension. This implies that the corresponding formula is derived under the assumption that the interfacial length in local coordinates follows the hyperbolic tangent profile. To confirm this numerically, the circumference of the ellipse is measured using the Dirac-delta function [40] and compared with the reference approximation $L$ based on the series solution i.e.

$$L = \pi(a + b)\left(1 + \frac{3s}{10 + \sqrt{4 - 3s}}\right), \qquad (2.6)$$

where $s = (a - b)^2/(a + b)^2$. We choose the Dirac-delta function as $|\nabla\phi|$. Table 1 shows the circumference of ellipse before and after the modification.
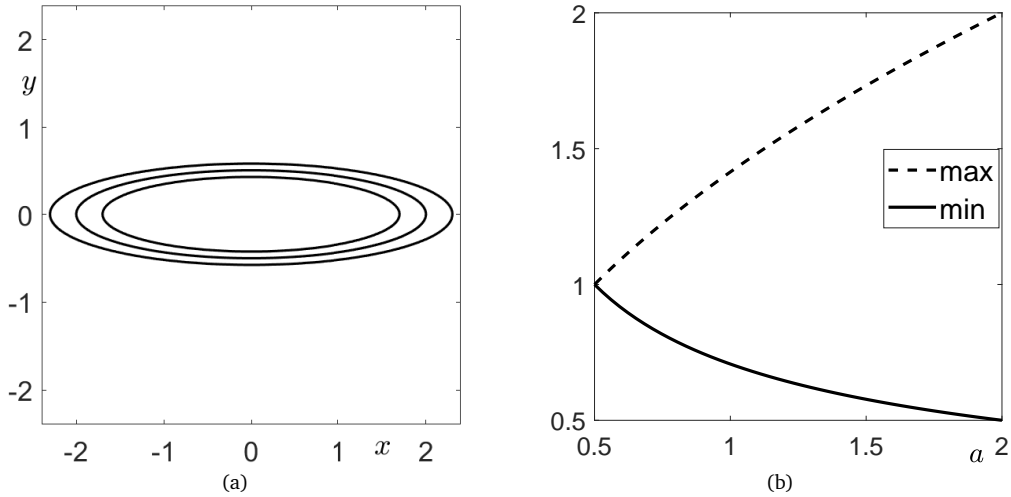


Figure 16: (a) Contour plot of Eq. (2.5) at the levels $\phi = -0.9, 0, 0.9$. (b) The scaled maximum ($\sqrt{a/b}$) and minimum ($\sqrt{b/a}$) of the transition width against $a$ with $b$.
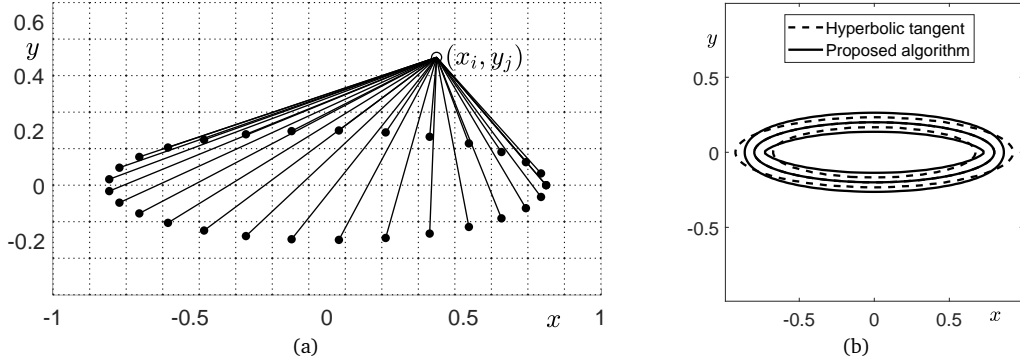
Figure 17: (a) Schematic of defining distance function. (b) An example of contour plot of general ellipse (dashed line) and ellipse obtained from the proposed algorithm (solid line).

Now, we discuss how to make an ellipse whose contours are uniform in any direction. Spreading $n$ points over the ellipse, we measure the distance from a fixed point $(x_i, y_j)$ to the every chosen point and denote the minimum value by $d_{ij}$. If $x_i^2/a^2 + y_j^2/b^2 > 1$ (outside the ellipse), then redefine the distance as $d_{ij} := -d_{ij}$. Repeat these steps for all $i$ and $j$, and we finally set $\phi_{ij}^0 = \tanh(d_{ij}/(\sqrt{2}\epsilon))$. See Fig. 17(a) for the schematic illustration of defining distance function and Fig. 17(b) for the result using the proposed algorithm. As Figs. 16(a) and 17(b) show, the ellipse used only tanh function has uneven thickness at each level. Conversely, the ellipse applied our proposed method has uniform thickness at each level, regardless of the horizontal or vertical direction.

Table 1: Circumference of ellipse with uniform and non-uniform interfacial thickness.

| Types | Uniform | Non-uniform | Reference |
|---|---|---|---|
| Circumference | 3.4315 | 3.4301 | 3.4314 |

### 2.4.2. Multiple isolated circles with random radius

In the two-dimensional space we consider the following initial condition composed of $k$ isolated circles:

$$\phi(x, y, 0) = k - 1 + \sum_{i=1}^{k} \tanh\left(\frac{r_i - \sqrt{(x - x_i)^2 + (y - y_i)^2}}{\sqrt{2}\epsilon}\right), \tag{2.7}$$

where $(x_i, y_i)$ and $r_i = 0.2\text{rand}$ are the center of the $i$-th circle and its random radius. Recall that "rand" are uniformly distributed random numbers between 0 and 1. In Fig. 18, we present 10 isolated circles on $\Omega = (-1, 1) \times (-1, 1)$ with arbitrary radii. Here, uniform mesh size $h = 1/64$ and $\epsilon = \epsilon_2$ are used. We can see the mesh plot of the phase-field $\phi(x, y, 0)$ which has the values between $-1$ and $1$, cf. Fig. 18(a). Furthermore, we can observe the zero-level contours $\phi(x, y, 0)$ in Fig. 18(b).
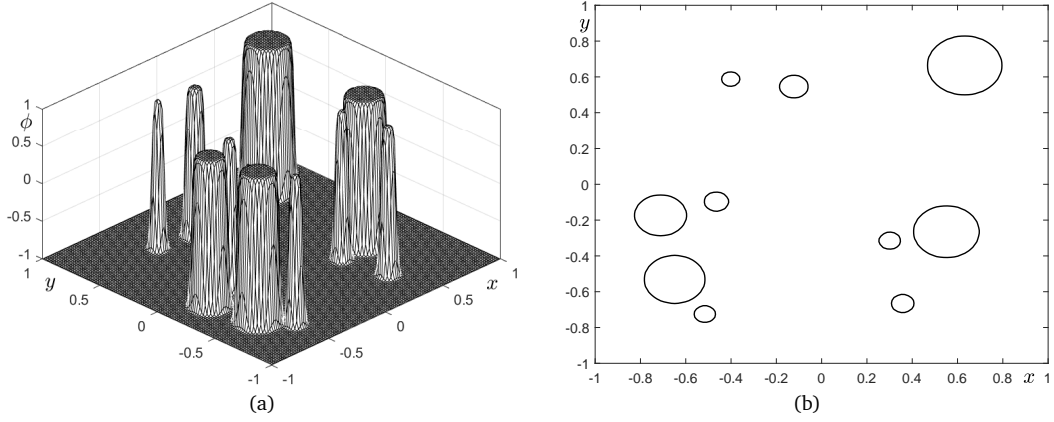
Figure 18: Multiple isolated circles with random radius in the two-dimensional space: (a) mesh plot of the phase-field $\phi(x, y, 0)$ and (b) its zero-level contour.

### 2.4.3. Sinusoidal profile

For the initial condition of the RT instability problems [41], sinusoidal profiles are used. Because the RT instability usually requires only a very small perturbation — i.e. a small amplitude, an initial condition can be set by the following equation:

$$\phi(x, y, 0) = \tanh\left(\frac{y - 0.01\cos(2\pi x)}{\sqrt{2}\epsilon}\right), \tag{2.8}$$

where $\epsilon$ is a width of interface and $\epsilon = \epsilon_8$. However, if we consider large perturbations and uniform thickness at each level, then (2.8) is not suitable for initial condition profiles. Contour lines of (2.8) are not uniform. Nevertheless, applying the method used for the ellipse, we arrive at uniform contour lines — cf. Fig. 19.
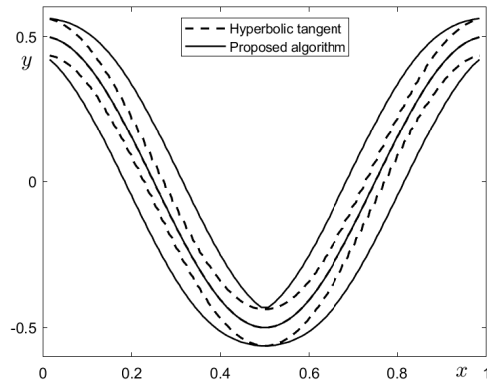


Figure 19: Contour lines at $\phi = -0.9, 0, 0.9$ using Eq. (2.8) (dashed line) and the proposed algorithm (solid line).

### 2.4.4. Sphere and ellipsoid

In this section, we consider the initial conditions for a sphere [22] and an ellipsoid [18]. The initial condition for sphere

$$\phi(x, y, z, 0) = \tanh\left(\frac{r - \sqrt{x^2 + y^2 + z^2}}{\sqrt{2}\epsilon}\right) \tag{2.9}$$

is defined on $\Omega = (-1.2, 1.2)^3$. Fig. 20(a) shows the initial phase condition for sphere at the levels $-0.9, 0$, and $0.9$. Here, $r = 1$, $h = 2.4/128$, $\epsilon = \epsilon_8$, and the mesh grid $N_x \times N_y \times N_z = 128 \times 128 \times 128$ are used.

To be consistent with the Eq. (2.9), for the ellipsoid, we consider the following form in 3D space $\Omega = (-2.4, 2.4) \times (-1.2, 1.2) \times (-1.2, 1.2)$:

$$\phi(x, y, z, 0) = \tanh\left(\frac{\sqrt[3]{abc} - \sqrt[3]{abc}\sqrt{x^2/a^2 + y^2/b^2 + z^2/c^2}}{\sqrt{2}\epsilon}\right). \tag{2.10}$$

Fig. 20(b) shows the isosurfaces of the ellipsoidal initial condition at the levels $\phi = -0.9, 0$ and $0.9$ with $a = 2.1$, $b = c = 0.7$, $\epsilon = \epsilon_8$, and the mesh grid $N_x \times N_y \times N_z = 256 \times 128 \times 128$.

Now, we also make an ellipsoid whose isosurfaces are uniform in any direction. First, spread $n$ points over the ellipsoid, measure the distance from a fixed point $(x_i, y_j, z_k)$ to every point on the surface and denote the minimum of the distances by $d_{ijk}$. If $x_i^2/a^2 + y_j^2/b^2 + z_k^2/c^2 > 1$ (outside the ellipsoid), redefine that value as $d_{ijk} := -d_{ijk}$. Repeat these
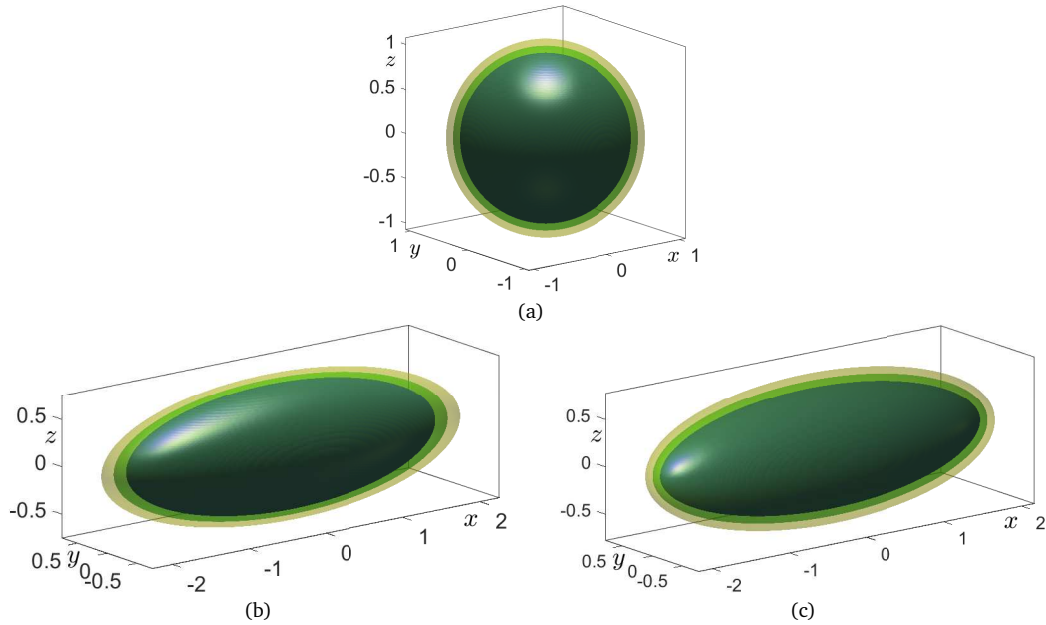


Figure 20: (a) Isosurface of Eq. (2.9) at the levels $\phi = -0.9, 0$, and $0.9$. (b) Isosurface of Eq. (2.10) at the levels $\phi = -0.9, 0$, and $0.9$. (c) Isosurface of proposed algorithm at the levels $\phi = -0.9, 0$, and $0.9$.

steps for all $i, j$, and $k$, and set $\phi_{ijk} = \tanh(d_{ijk}/(\sqrt{2}\epsilon))$. Fig. 20(c) shows the initial condition for ellipsoid at the levels $\phi = -0.9, 0$, and $0.9$ obtained by the proposed algorithm. Similar to the ellipse case, the thickness between levels in any directions is not the same. However, the ellipsoid obtained by our algorithm has uniform isosurfaces in any direction.

### 2.4.5. Torus

We now consider a torus. This is the surface of revolution generated by revolving a circle in 3D space about an axis. The radius $R$ of the large circle is known as the major radius and the radius $r$ of the small one is the minor radius. The authors of [18] consider both ellipsoid and torus as initial conditions. There are two kinds of tori — viz. symmetric and non-symmetric ones. An initial condition for the torus at the center $(0, 0, 0)$ and on $\Omega = (-1.5, 1.5) \times (-1.5, 1.5) \times (-0.75, 0.75)$ has the form

$$\phi(x, y, z, 0) = \tanh\left(\frac{r^2 - \left(R - \sqrt{x^2 + y^2}\right)^2 - z^2}{\sqrt{2}\epsilon}\right). \tag{2.11}$$

Fig. 21(a) shows the isosurface of $\phi$ at the levels $-0.9, 0, 0.9$ for the radially symmetric torus with $R = 0.6$ and $r = 0.3$ about the $z$-axis. Figs. 21(b) and 21(c) show the isosurfaces of $\phi$ at the levels $-0.9, 0, 0.9$ for the radially non-symmetric torus with $R = 0.6$, and $r = 0.05\sin(\arctan(y, x)) + 0.3$ about the $z$-axis, the Eq. (2.11) and the proposed algorithm, respectively. Here, we use $h = 3/128$, $\epsilon = \epsilon_4$, and the mesh grid $N_x \times N_y \times N_z = 128 \times 128 \times 64$.
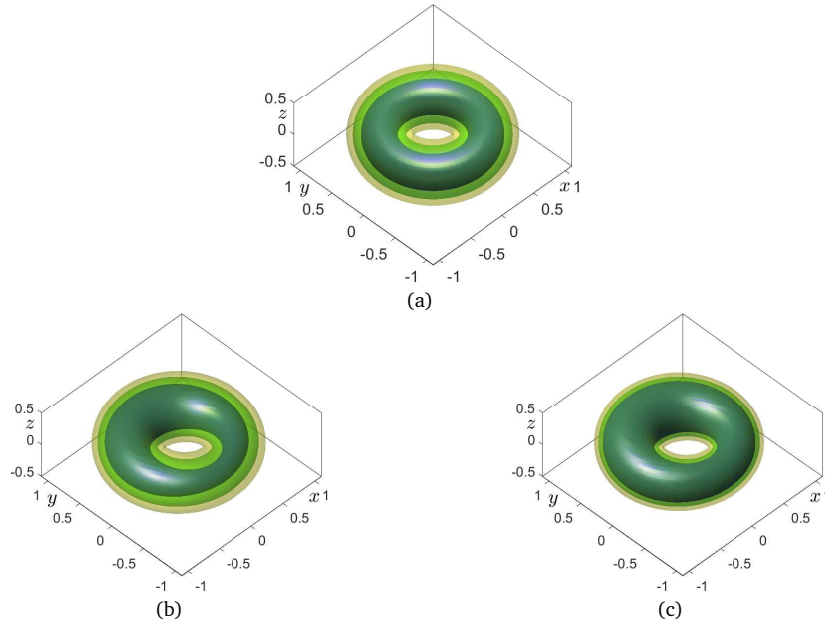


Figure 21: (a) is radially symmetric torus. (b) and (c) are radially non-symmetric tori about the $z$-axis with Eq. (2.11) and the proposed algorithm, respectively.

### 2.4.6. Triply periodic minimal surfaces

As the next step, we consider triply periodic minimal surfaces widely used in biotechnology. They are approximated by periodic nodal surfaces [27]. Let us present the periodic nodal surfaces approximations of triply periodic minimal surfaces, respectively, referred to as Schwarz primitive (P), Schwarz diamond (D), and Gyroid (G). More precisely, they are

$$\cos(2\pi x) + \cos(2\pi y) + \cos(2\pi z) = 0, \tag{2.12}$$

$$\cos(2\pi x)\cos(2\pi y)\cos(2\pi z) - \sin(2\pi x)\sin(2\pi y)\sin(2\pi z) = 0, \tag{2.13}$$

$$\sin(2\pi x)\cos(2\pi y) + \sin(2\pi z)\cos(2\pi x) + \sin(2\pi y)\cos(2\pi z) = 0, \tag{2.14}$$

where $x, y, z \in [0, 1]$. Note that these periodic representations do not match the Euclidean distance, which causes problems for establishing the equilibrium profile. One of possible solutions is to use the cut-off and relaxation — cf. [57]. Figs. 22(a)-(22c) show the periodic nodal surfaces approximations of P, D, and G surfaces, and Figs. 22(d)-22(f) demonstrate the reconstructed approximations of P, D, and G surfaces, followed by Step 1 to 6 in [57].
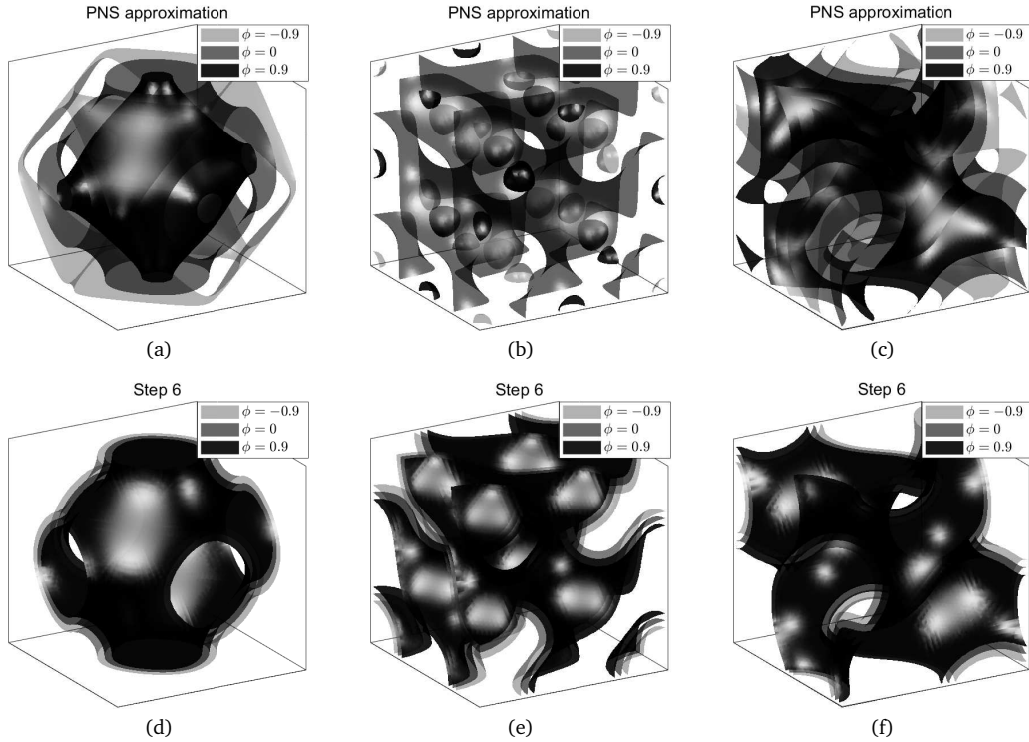


Figure 22: (a)-(c) are the periodic nodal surfaces approximations of P, D, and G surfaces, respectively, which are represented by Eqs. (2.12)-(2.14). (d)-(f) are reconstructed profile of P, D, and G surfaces which can be employed to the initial conditions for the phase-field models. The process is followed by Step 1 to 6 in [57].

## 2.5. Periodic waves on curve and surface

Initially periodic waves on closed curves or surfaces are often provided to study mean curvature flows and dendrite pattern formation [42]. To achieve this perturbation in inceptive period, one can use polar and spherical harmonics [14]. The polar harmonics in real parts, or $k$-fold symmetries have the form

$$W_k(\theta) = \cos\left(k(\theta - \theta_{ref})\right),$$

where $k$ is the number of symmetric tips, $\theta = \arctan(y/x) + \pi I(x < 0)$, and $\theta_{ref}$ is a given angle. Note that $I(\cdot)$ is an indicator function. Fig. 23 displays the initial states including periodic waves on curves. We use the following equation

$$\phi(x, y, 0) = \tanh\left(\frac{r + AW_k - \sqrt{x^2 + y^2}}{\sqrt{2}\epsilon}\right),$$

where $(x, y) \in [-0.9, 0.9]^2$, $r$ is the circle radius, and $A$ the amplitude of the wave. Consequently, the spherical harmonics in real parts are given as

$$Y_l^m(\theta, \phi) = \sqrt{\frac{(2l+1)(l-m)!}{4\pi(l+m)!}} P_l^m(\cos\theta)\sin(m\phi),$$

where $l$ is the degree of the wave in the latitudinal coordinates with $\theta = \arctan(y/x)I(y > 0) + \pi I(x < 0)$, i.e. $\theta \in [0, \pi]$, and $m$ is the order of the wave in longitudinal coordinate with $\phi = \text{sgn}(y)\arccos(z/\sqrt{x^2 + y^2 + z^2}) + \pi$, i.e. $\phi \in [0, 2\pi)$. Here, $P_l^m(\cdot)$ is an associated Legendre polynomial. Fig. 24 shows the initial states, including periodic waves on surfaces. We employ the following equation:

$$\phi(x, y, z, 0) = \tanh\left(\frac{r + AY_l^m - \sqrt{x^2 + y^2 + z^2}}{\sqrt{2}\epsilon}\right),$$
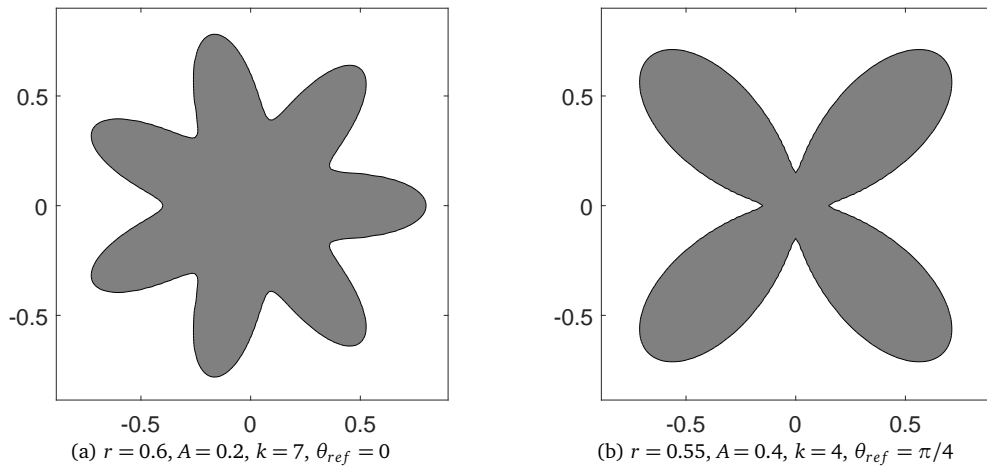
where $(x, y, z) \in [-1.2, 1.2]^3$.



(a) $r = 0.6$, $A = 0.2$, $k = 7$, $\theta_{ref} = 0$          (b) $r = 0.55$, $A = 0.4$, $k = 4$, $\theta_{ref} = \pi/4$

Figure 23: Polar harmonics on curves.

(a) $r = 0.8$, $A = 0.8$, $l = 15$, $m = 7$ (b) $r = 0.7$, $A = 0.5$, $l = 8$, $m = 5$
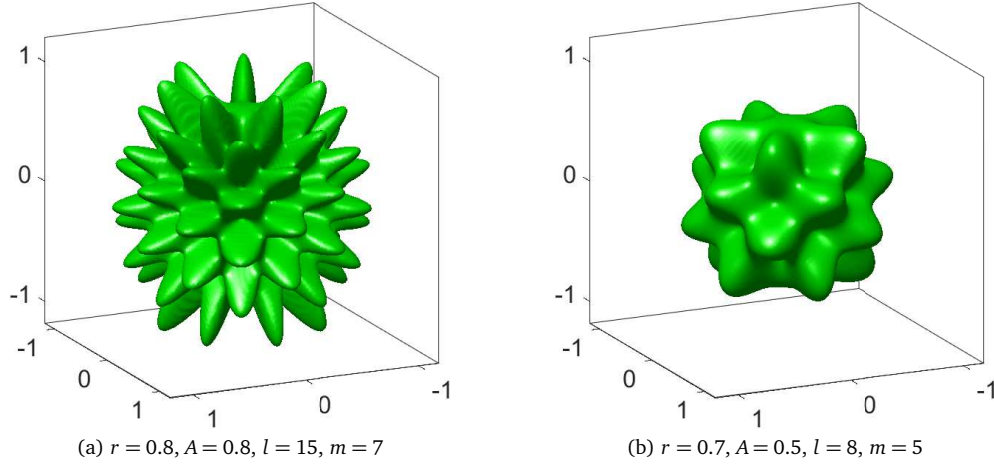
Figure 24: Spherical harmonics on spheres.

## 2.6. Initial conditions with the same total concentration

Let us make initial conditions for circle and ellipse having the same area. For example, if the circle radius is $r$ and the ellipse major and minor axes are $a$ and $b$, then the areas are $\pi r^2$ and $\pi a b$, respectively. As a concrete example, we consider $r = 1$, $a = 2$, and $b = 0.5$. For these parameters, both figures have the area $\pi$. For approximate solutions, however, numerical areas are different. We set two conditions using tanh function in $(-2.4, 2.4) \times (-2.4, 2.4)$ with the mesh grid $128 \times 128$, viz. the one $\phi_{ij}^c$ meaning the circle of radius $r = 1$ at the zero level, and another $\phi_{ij}^e$ meaning the ellipse with $a = 2$ and $b = 0.5$ at the zero level

$$\phi_{ij}^c = \tanh\left(\frac{1 - \sqrt{x^2 + y^2}}{\sqrt{2}\epsilon}\right),$$

$$\phi_{ij}^e = \tanh\left(\frac{1 - \sqrt{x^2/4 + 4y^2}}{\sqrt{2}\epsilon}\right).$$

Figs. 25(a) and 25(b) show the mesh for $\phi_{ij}^c$ with $r = 1$ and $\phi_{ij}^e$ with $a = 2$ and $b = 0.5$, respectively.

Generally, the total concentration for $\phi_{ij}^c$ and $\phi_{ij}^e$ is different, viz.

$$\sum_{i=1}^{N_x}\sum_{j=1}^{N_y} \phi_{ij}^c \neq \sum_{i=1}^{N_x}\sum_{j=1}^{N_y} \phi_{ij}^e.$$

We use the following correction in order to have the same total concentration for the ellipse and circle:

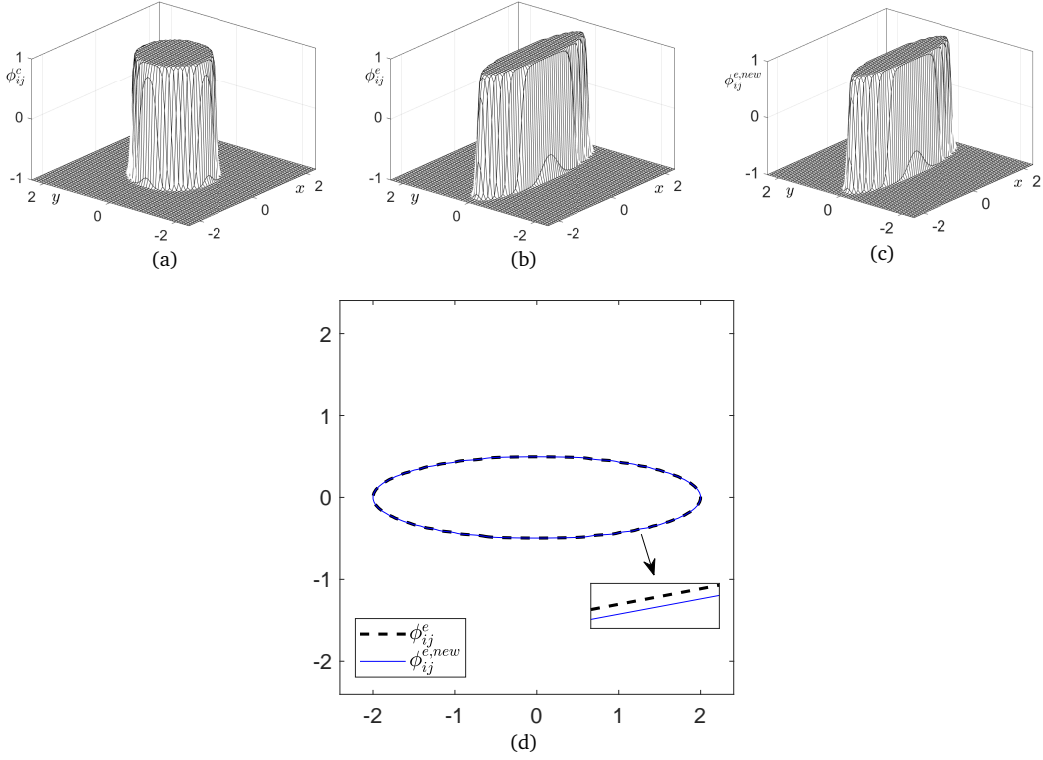$$\phi_{ij}^{e,new} = \phi_{ij}^e + \alpha F(\phi_{ij}^e),$$

Figure 25: (a) Mesh of $\phi_{ij}^c$. (b) Mesh of $\phi_{ij}^e$. (c) Total concentration corrected ellipse, $\phi_{ij}^{e,new}$. (d) Contours of $\phi_{ij}^e$ and $\phi_{ij}^{e,new}$ at zero-level.

where $\alpha$ is a constant and $F(\phi) = 0.25(\phi^2 - 1)^2$. $F(\phi) = 0.25(\phi^2 - 1)^2$ the double well potential energy. To find $\alpha$, we set

$$\sum_{i=1}^{N_x}\sum_{j=1}^{N_y}\phi_{ij}^c = \sum_{i=1}^{N_x}\sum_{j=1}^{N_y}\phi_{ij}^{e,new} = \sum_{i=1}^{N_x}\sum_{j=1}^{N_y}\left[\phi_{ij}^e + \alpha F(\phi_{ij}^e)\right].$$

Then

$$\alpha = \frac{\sum_{i=1}^{N_x}\sum_{j=1}^{N_y}\left(\phi_{ij}^c - \phi_{ij}^e\right)}{\sum_{i=1}^{N_x}\sum_{j=1}^{N_y}F\left(\phi_{ij}^e\right)}.$$

Using this $\alpha$, we can derive a new total concentration $\phi_{ij}^{e,new}$ which is closer to $\phi_{ij}^c$. The advantage this algorithm has is that it is able to reduce the error without losing the concentration. Fig. 25(c) shows the mesh $\phi_{ij}^{e,new}$ similar to $\phi_{ij}^e$. However, as shown in Fig. 25(d), two contours of $\phi_{ij}^e$ and $\phi_{ij}^{e,new}$ at the zero-level differ when viewed closely. In fact, we got the numerical area of circle and ellipse as 3.1398 and 3.1384, respectively. The numerical area of the corrected ellipse is 3.1394, which is close to the area of circle.

## 2.7. Initial condition from an image

In this section, we use the image segmentation process in order to make initial conditions from an image — cf. [33]. The image segmentation method is based on the following equation:

$$\frac{\partial \phi(\mathbf{x}, t)}{\partial t} = g\big(f_0(\mathbf{x})\big)\left(-\frac{F'(\phi)}{\epsilon^2} + \Delta\phi\right) + \lambda g\big(f_0(\mathbf{x})\big)F(\phi),$$

where

$$f_0(\mathbf{x}) = \frac{f(\mathbf{x}) - f_{\min}}{f_{\max} - f_{\min}},$$

$g(f_0(\mathbf{x}))$ is an edge stopping function aimed to stop evolution when contour approaches an edge, and $f_{\max}$ and $f_{\min}$ are, respectively, the maximum and minimum values of a given image $f(\mathbf{x})$. In Fig. 26, we use $\lambda = 10^{-4}$, $\epsilon = \epsilon_4$, $h = 1/64$, $\Delta t = 10^{-5}$, and $64 \times 64$ mesh. We set $\phi(\mathbf{x}, 0)$ as $\phi(\mathbf{x}, 0) = -1$ if $\mathbf{x}$ is inside two square contour (green line) and $\phi(\mathbf{x}, 0) = 1$ otherwise (see the first column in Fig. 26). The initial data evolves until it reaches the boundary of the image through the motion by the mean curvature and the term $\lambda g(f_0(\mathbf{x}))F(\phi)$.
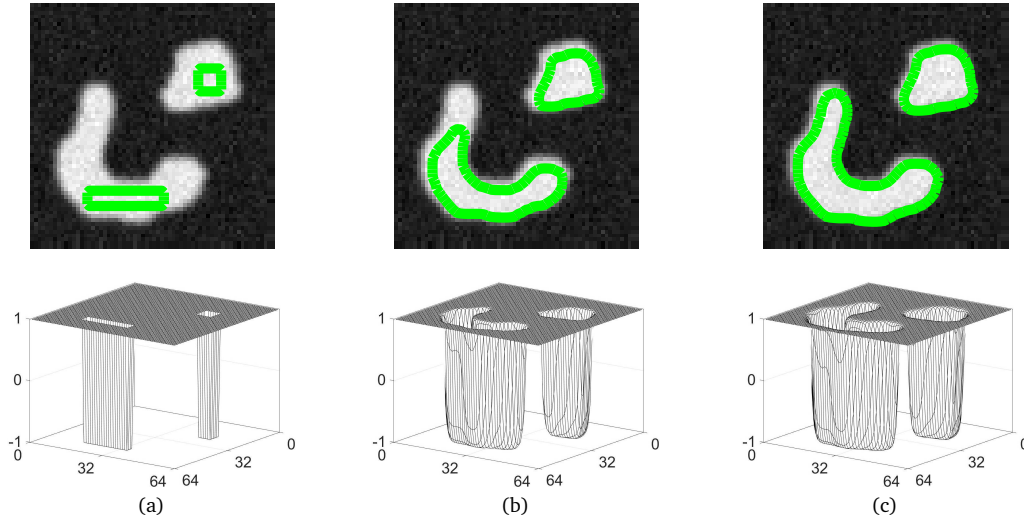


Figure 26: Image segmentation process at (a) 0 iteration, (b) 300 iterations, and (c) 1200 iterations.

## 2.8. Random initial conditions for multi-component mixture

In this part, we consider two random initial conditions for multi-component CH equations. Such equations can be written as

$$\frac{\partial c_i}{\partial t} = \nabla \cdot \big(M(\mathbf{c})\nabla\mu_i\big),$$
$$\mu_i = F'(c_i) - \epsilon^2 \Delta c_i + \beta(\mathbf{c}),$$

where $c_i$ and $\mu_i$ represent a specific mole fraction and the chemical potential for $i = 1, 2, \ldots, N$, $F(c_i) = 0.25c_i^2(1 - c_i)^2$. Let $M(\mathbf{c}) = M = 1$ be the constant mobility and

$$\beta(\mathbf{c}) = \frac{1}{N} \sum_{i=1}^{N} F'(c_i)$$

a Lagrange multiplier, which maintains the summation of total mole fractions to be 1, i.e. $c_1 + c_2 + \cdots + c_N = 1$ [4]. In numerical tests, we use $N = 5$ on $\Omega = (0, 1) \times (0, 1)$, $h = 1/128$, $\Delta t = 0.2h$, and $\epsilon = 0.0047$. The first initial condition is

$$c_1(x, y, 0) = 0.2 + 0.01\text{rand}, \quad c_2(x, y, 0) = 0.2 + 0.01\text{rand},$$
$$c_3(x, y, 0) = 0.2 + 0.01\text{rand}, \quad c_4(x, y, 0) = 0.2 + 0.01\text{rand},$$
$$c_5(x, y, 0) = 1 - c_1(x, y, 0) - c_2(x, y, 0) - c_3(x, y, 0) - c_4(x, y, 0),$$

where rand represents a random number between $-1$ and $1$. The second one is

$$c_1(x, y, 0) = 1, \quad c_2(x, y, 0) = \cdots = c_5(x, y, 0) = 0, \quad \text{if} \quad \text{rand}' < 1/5,$$
$$c_2(x, y, 0) = 1, \quad c_1(x, y, 0) = \cdots = c_5(x, y, 0) = 0, \quad \text{else if} \quad \text{rand}' < 2/5,$$
$$c_3(x, y, 0) = 1, \quad c_1(x, y, 0) = \cdots = c_5(x, y, 0) = 0, \quad \text{else if} \quad \text{rand}' < 3/5,$$
$$c_4(x, y, 0) = 1, \quad c_1(x, y, 0) = \cdots = c_5(x, y, 0) = 0, \quad \text{else if} \quad \text{rand}' < 4/5,$$
$$c_5(x, y, 0) = 1, \quad c_1(x, y, 0) = \cdots = c_4(x, y, 0) = 0, \quad \text{otherwise},$$

where rand$'$ represents the random number between 0 and 1. For convenience, the Case 1 and Case 2 are used to indicate the first and second initial conditions, respectively.

Figs. 27(a) and 27(c) show the initial condition of $c_1$ for Case 1 and Case 2, whereas Figs. 27(b) and 27(d) demonstrate corresponding evolutional results for $c_1$ at $t = 1.4063$. We can observe that the initial perturbation of Case 1 becomes flat with time. On the other hand, in Case 2 the phase separation evolves. Therefore, Case 2 is preferable for the simulation of the multi-component phase separation with randomly distributed initial conditions.

## 2.9. Initial condition using Voronoi diagram

The Voronoi diagram splits a given domain with seed points into disjoint polygons. There is one polygon consisting of all points closer to that seed point than any others for each seed point. Fig. 28 shows the result of evolution with a certain initial condition [54].

This suggests that the use of the Voronoi diagram as an initial condition can be more efficient and natural in order to obtain the local equilibrium solution in multi-component phase-field models. This is because the final shape of separation is the union of Voronoi polygons. Let us consider $N$-component phase-field system, i.e. $c_1, c_2, \ldots, c_N$. Let $(X_l, Y_l)$, $l = 1, \ldots, M$ be the seed points. For all $l = 1, \ldots, M$, we assign 1 to a randomly chosen concentration field and 0 to the other concentration fields for the polygon including a seeding point. For example, let $M = 4$, then for some grid point $(x_i, y_j)$ we compute the distances
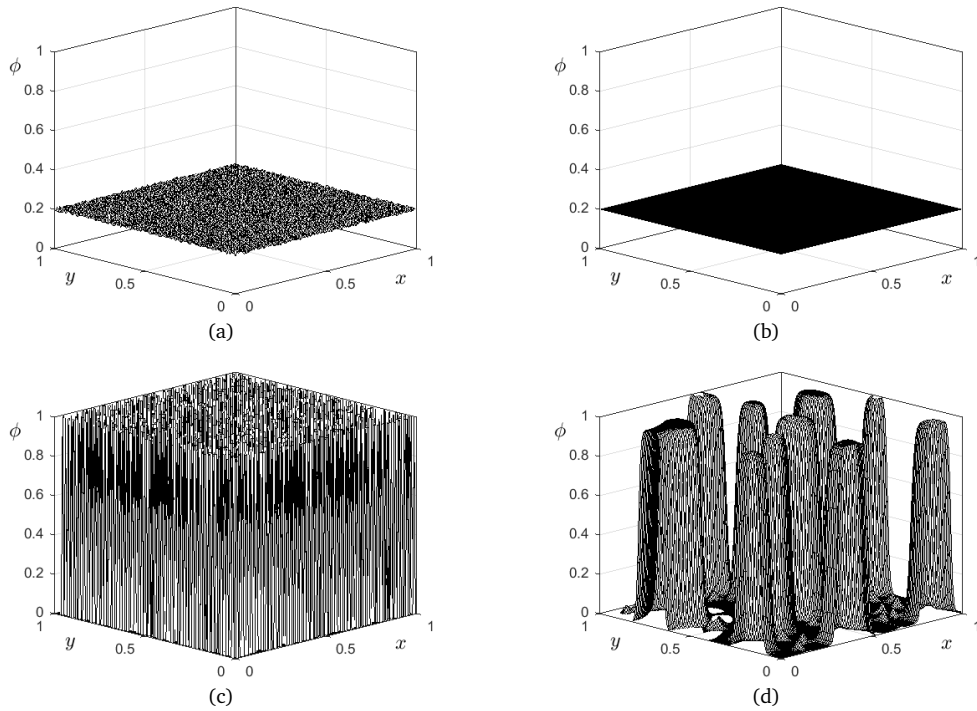
Figure 27: Temporal evolutions with two different initial conditions. (a) and (c) are the initial conditions of $c_1$ for Case 1 and Case 2. (b) and (d) are the corresponding evolutional results of $c_1$ at $t = 1.4063$.

$d_l$ between the grid point and the seed points, $(X_l, Y_l)$, for $l = 1, 2, 3, 4$. Find the index $l$ which makes the minimum distance and assign one to the index $l$-associated concentration field and zero to the other concentration fields — cf. Fig. 29(a). We loop over all grid points to define values of the phase-fields. Figs. 29(b) and 29(c) show 30 seed points and the resulting Voronoi diagram using the above procedure.

Figs. 30(a)-30(d) show mesh plots with four phase-fields for a simplicity.



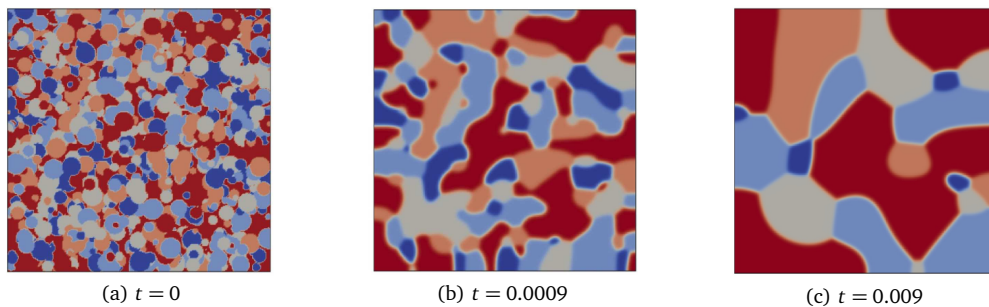(a) $t = 0$      (b) $t = 0.0009$      (c) $t = 0.009$

Figure 28: Result of evolution to morphologies during a spinodal phase separation of 5-component system with average composition. Reprinted from [54] with permission of Elsevier Science. For interpretation of the colors in the figures, the reader is referred to the web version of this article.
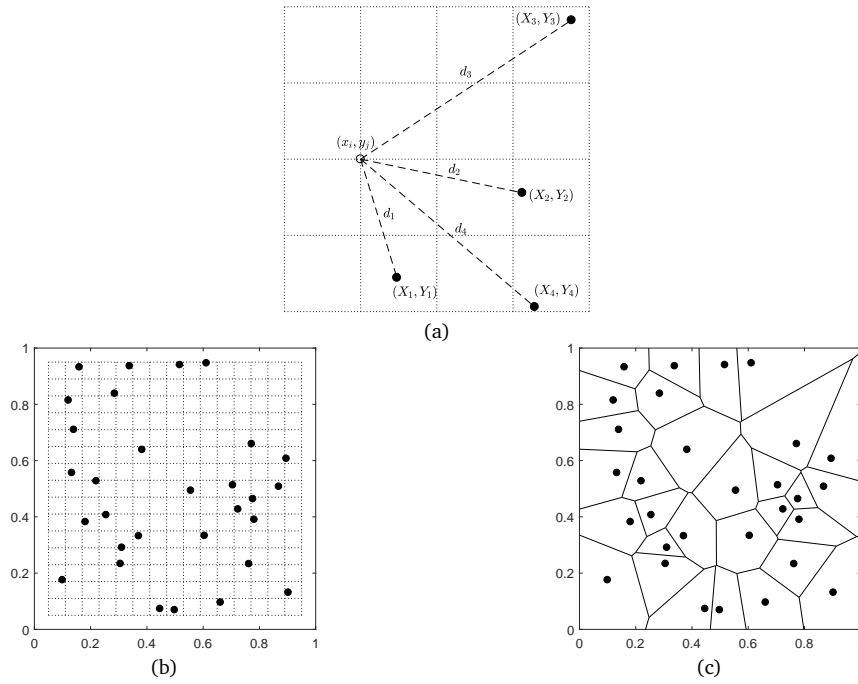
(a)



(b)



(c)

Figure 29: (a) Schematic illustration of assigning a concentration value to a grid point in 2D. (b) 30 seed points. (c) Voronoi diagram.
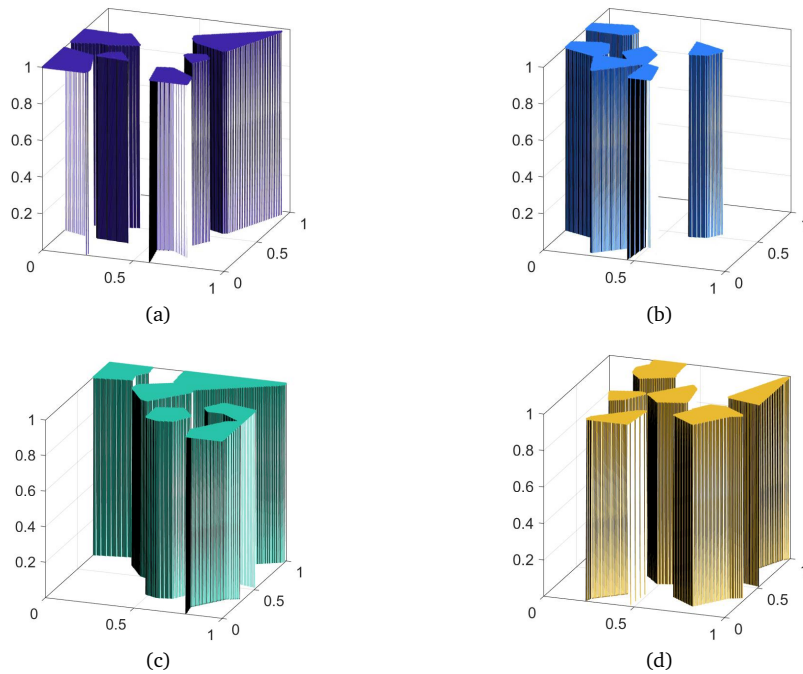


(a)



(b)



(c)



(d)

Figure 30: (a), (b), (c), and (d) are mesh plots for concentrations $c_1, c_2, c_3$, and $c_4$, respectively.
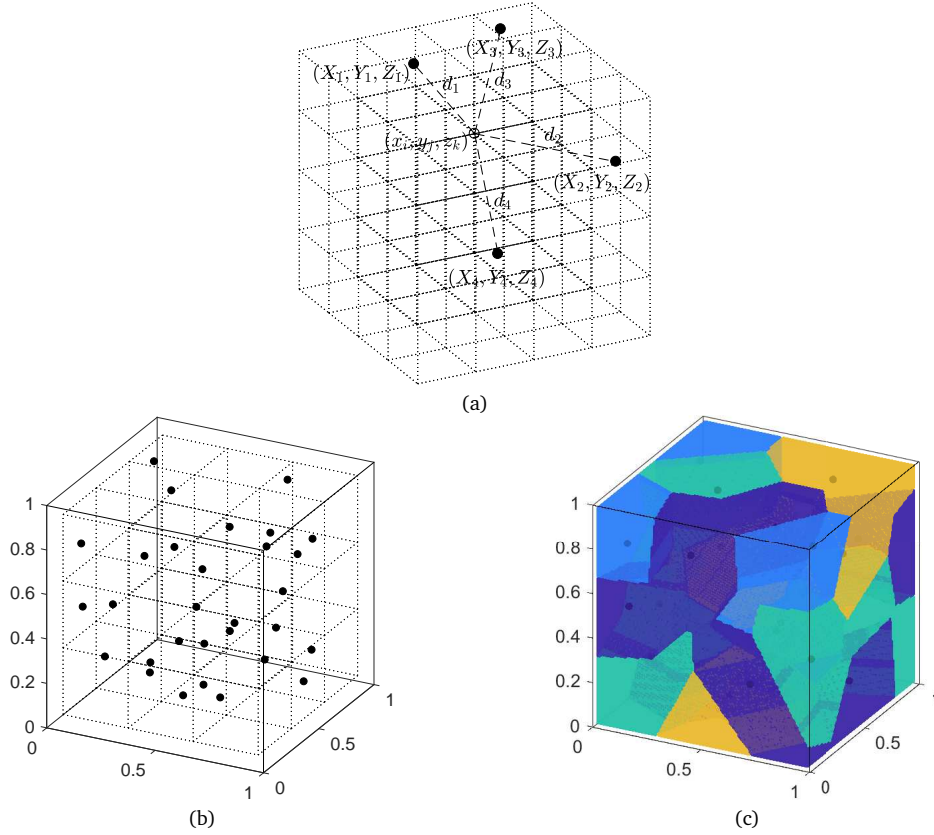
Figure 31: (a) Schematic illustration of assigning a concentration value to a grid point in 3D. (b) 30 random seed points in 3D space. (c) Resulting 3D Voronoi diagram.

Three-dimensional Voronoi tessellations have been used in the grain growth simulation. The 2D procedure can be directly extended to 3D procedure for generating 3D Voronoi diagram. Fig. 31 schematically illustrates the assignment of the concentration value to a grid point, 30 random seed points, and the resulting Voronoi diagram.

Fig. 32 shows the isosurfaces at the 1/2 level for the concentrations $c_1, c_2, c_3$, and $c_4$, respectively.

## 3. Conclusions

In order to correctly calculate interfacial dynamics numerically and physically, it is important to choose adequate initial guesses. In this work, we discuss how to chose proper initial conditions in simulations of phase-field models. In particular, defining a level set via a signed distance field is essential for phase-field models on curved surfaces. If various basic physics laws such as preserving the mass and decreasing energy should be satisfied, the constraints can be employed by reflecting the initial conditions.
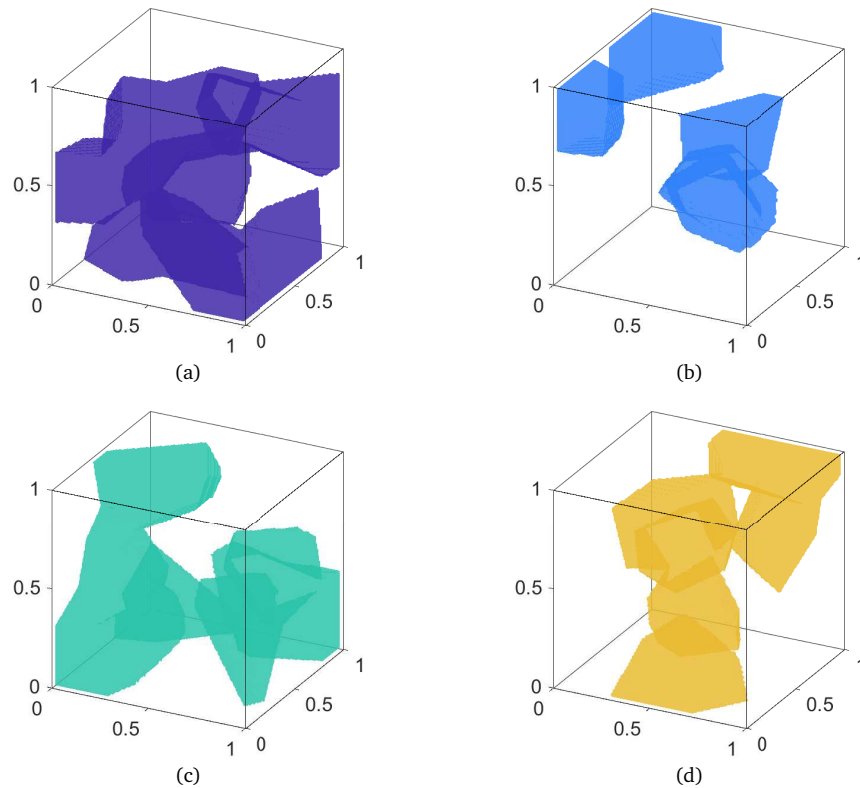
Figure 32: (a), (b), (c), and (d) are isosurfaces at the $1/2$ level for concentrations $c_1, c_2, c_3$, and $c_4$, respectively.

## Acknowledgments

## References

[1] E. Ahmed, J. Jaffré and J.E. Roberts, *A reduced fracture model for two-phase flow with different rock types*, Math. Comput. Simul. **137**, 49–70 (2017).

[2] S.M. Allen and J.W. Cahn, *A microscopic theory for antiphase boundary motion and itst application to antiphase domain coarsening*, Acta Mater. **27**, 1085–1095 (1979).

[3] F.O. Alpak, B. Riviere and F. Frank, *A phase-field method for the direct simulation of two-phase flows in pore-scale media using a non-equilibrium wetting boundary condition*, Comput. Geosci. **20**, 881–908 (2016).

[4] J. Bosch and M. Stoll, *Preconditioning for vector-valued Cahn–Hilliard equations*, SIAM J. Sci. Comput. **37**, S216–S243 (2015).

[5] A.L. Brkić and A. Novak, *A nonlocal image inpainting problem using the linear Allen–Cahn equation*, In Conference on Non-integer Order Calculus and Its Applications, pp. 229–239, Springer (2018).

[6] T.A. Bubba, D. Labate, G. Zanghirati and S. Bonettini, *Shearlet-based regularized reconstruction in region-of-interest computed tomography*, Math. Model. Nat. Pheno. **13**, 34 (2018).

[7] J.W. Cahn, *On spinodal decomposition*, Acta Mater. **9**, 795–801 (1961).

[8] J.W. Cahn and J.E. Hilliard, *Spinodal decomposition: A reprise*, Acta Mater. **19**, 151–161 (1971).

[9] K.F. Casey, *Periodic traveling-wave solutions to the Whitham equation*, Math. Model. Nat. Pheno. **13**, 16 (2018).

[10] Z. Chai, D. Sun, H. Wang and B. Shi, *A comparative study of local and nonlocal Allen-Cahn equations with mass conservation*, Int. J. Heat Mass Transf. **122**, 631–642 (2018).

[11] Q. Cheng, X. Yang and J. Shen, *Efficient and accurate numerical schemes for a hydro-dynamically coupled phase field diblock copolymer model*, J. Comput. Phys. **341**, 44–60 (2017).

[12] J.M. Church, Z. Guo, P.K. Jimack, A. Madzvamuse, K. Promislow, B. Wetton, S.M. Wise and F. Yang, *High accuracy benchmark problems for Allen-Cahn and Cahn-Hilliard dynamics*, Commun. Comput. Phys. **26**, 947–972 (2019).

[13] P. Colli, G. Gilardi and J. Sprekels, *A distributed control problem for a fractional tumor growth model*, Mathematics **7**, 792 (2019).

[14] V. Cristini and J. Lowengrub, *Three-dimensional crystal growth-II: nonlinear simulation and control of the Mullins-Sekerka instability*, J. Cryst. Growth **266**, 552–567 (2004).

[15] S. Dai and Q. Du, *Computational studies of coarsening rates for the Cahn-Hilliard equation with phase-dependent diffusion mobility*, J. Comput. Phys. **310**, 85–108 (2016).

[16] M. Dehghan and M. Abbaszadeh, *The meshless local collocation method for solving multi-dimensional Cahn-Hilliard, Swift-Hohenberg and phase field crystal equations*, Eng. Anal. Bound. Elem. **78**, 49–64 (2017).

[17] G. Demange, M. Chamaillard, H. Zapolsky, M. Lavrskyi, A. Vaugeois, L. Luneville, D. Simeone and R. Patte, *Generalization of the Fourier-spectral Eyre scheme for the phase-field equations: Application to self-assembly dynamics in materials*, Comput. Mater. Sci. **144**, 11–22 (2018).

[18] Q. Du, C. Liu and X. Wang, *Simulating the deformation of vesicle membranes under elastic bending energy in three dimensions*, J. Comput. Phys. **212**, 757–777 (2006).

[19] M. Dziwnik, A. Münch and B. Wagner, *An anisotropic phase-field model for solid-state dewetting and its sharp-interface limit*, Nonlinearity **30**, 1465 (2017).

[20] K.R. Elder and M. Grant, *Modeling elastic and plastic deformations in nonequilibrium processing using phase field crystals*, Phys. Rev. E **70**, 051605 (2004).

[21] K.R. Elder, M. Katakowski, M. Haataja and M. Grant, *Modeling elasticity in crystal growth*, Phys. Rev. Lett. **88**, 245701 (2002).

[22] A. Fakhari, M. Geier and D. Bolster, *A simple phase-field model for interface tracking in three dimensions*, Comput. Math. Appl., (2016).

[23] A. Fakhari, M. Geier and D. Bolster, *A simple phase-field model for interface tracking in three dimensions*, Comput. Math. Appl. **78**, 1154–1165 (2019).

[24] A. Fasano and M. Primicerio, *Free Boundary Problems: Theory and Applications*, Pitman Advanced (1983).

[25] W. Feng, Z. Guan, J. Lowengrub, C. Wang, S.M. Wise and Y. Chen, *A uniquely solvable, energy stable numerical scheme for the functionalized Cahn-Hilliard equation and its convergence analysis*, J. Sci. Comput. **76**, 1938–1967 (2018).

[26] R. Gabbrielli, *Foam Geometry and Structural Design of Porous Material*, Ph. D. Thesis, University of Bath (2009).

[27] P.J. Gandy, S. Bardhan, A.L. Mackay and J. Klinowski, *Nodal surface approximations to the P, G, D and I-WP triply periodic minimal surfaces*, Chem. Phys. Lett. **336**, 187–195 (2001).

[28] H. Gomez, A. Reali and G. Sangalli, *Accurate, efficient, and (iso) geometrically flexible collocation methods for phase-field models*, J. Comput. Phys. **262**, 153–171 (2014).

[29] R. Guo and Y. Xu, *A high order adaptive time-stepping strategy and local discontinuous Galerkin method for the modified phase field crystal equation*, Commun. Comput. Phys. **24**, 123–151 (2018).

[30] Z. Guo, P. Lin, J. Lowengrub and S.M. Wise, *Mass conservative and energy stable finite difference methods for the quasi-incompressible Navier-Stokes-Cahn-Hilliard system: Primitive variable and projection-type schemes*, Comput. Methods Appl. Mech. Eng. **326**, 144–174 (2017).

[31] Q.A. Huang, W. Jiang and J.Z. Yang, *An efficient and unconditionally energy stable scheme for simulating solid-state dewetting of thin films with isotropic surface energy*, Comput. Phys **26**, 1444 (2019).

[32] D. Jeong and J. Kim, *Conservative Allen-Cahn-Navier-Stokes system for incompressible two-phase fluid flows*, Comput. Fluids **156**, 239–246 (2017).

[33] D. Jeong and J. Kim, *An explicit hybrid finite difference scheme for the Allen-Cahn equation*, J. Comput. Appl. Math. **340**, 247–255 (2018).

[34] D. Jeong and J. Kim, *Fast and accurate adaptive finite difference method for dendritic growth*, Comput. Phys. Commun. **236**, 95–103 (2019).

[35] W. Jiang, W. Bao, C.V. Thompson and D.J. Srolovitz, *Phase field approach for simulating solid-state dewetting problems*, Acta Mater. **60**, 5578-5592 (2012).

[36] W. Jiang, Q. Zhao and W. Bao, *Sharp-interface model for simulating solid-state dewetting in three dimensions*, SIAM J. Appl. Math. **80**, 1654–1677 (2020).

[37] V. Joshi and R.K. Jaiman, *A positivity preserving and conservative variational scheme for phase-field modeling of two-phase flows*, J. Comput. Phys. **360**, 137–166 (2018).

[38] K.B. Khattri and S.P. Pudasaini, *Channel flow simulation of a mixture with a full-dimensional generalized quasi two-phase model*, Math. Comput. Simul. **165**, 280–305 (2019).

[39] J. Langer, *Models of pattern formation in first-order phase transitions*, Directions in Condensed Matter Physics: Memorial Volume in Honor of Shang-Keng Ma pp. 165–186, World Scientific (1986).

[40] H.G. Lee and J. Kim, *Regularized Dirac delta functions for phase field models*, Int. J. Numer. Meth. Eng. **91**, 269–288 (2012).

[41] H.G. Lee and J. Kim, *A comparison study of the Boussinesq and the variable density models on buoyancy-driven flows*, J. Eng. Math. **75**, 15–27 (2012).

[42] Y. Li, H.G. Lee, D. Jeong and J. Kim, *An unconditionally stable hybrid numerical method for solving the Allen-Cahn equation*, Comput. Math. Appl. **60**, 1591–1606 (2010).

[43] F. Liu and J. Shen, *Stabilized semi-implicit spectral deferred correction methods for Allen-Cahn and Cahn-Hilliard equations*, Math. Methods Appl. Sci. **38**, 4564–4575 (2015).

[44] V. Mohammadi and M. Dehghan, *Simulation of the phase field Cahn-Hilliard and tumor growth models via a numerical scheme: Element-free Galerkin method*, Comput. Methods Appl. Mech. Eng. **345**, 919–950 (2019).

[45] C.-L. Park, J. Gibbs, P.W. Voorhees and K. Thornton, *Coarsening of complex microstructures following spinodal decomposition*, Acta Mater. **132**, 13–24 (2017).

[46] J. Shen and X. Yang, *Numerical approximations of Allen-Cahn and Cahn-Hilliard equations*, Discrete Contin. Dyn. Syst. **28**, 1669–1691 (2010).

[47] J. Shin, D. Jeong, Y. Li, Y. Choi and J. Kim, *A hybrid numerical method for the phase-field model of fluid vesicles in three-dimensional space*, Int. J. Numer. Methods Fluids **78**, 63–75 (2015).

[48] J. Shin, H.G. Lee and J.-Y. Lee, *Convex splitting Runge-Kutta methods for phase-field models*,

Comput. Math. Appl. **73**, 2388–2403 (2017).

[49] J. Swift and P.C. Hohenberg, *Hydrodynamic fluctuations at the convective instability*, Phys. Rev. A **15**, 319 (1977).

[50] N. Talat, B. Mavrič, V. Hatić, S. Bajt and B. Šarler, *Phase field simulation of Rayleigh-Taylor instability with a meshless method*, Eng. Anal. Bound. Elem. **87**, 78–89 (2018).

[51] R. Tavakoli, *Unconditionally energy stable time stepping scheme for Cahn-Morral equation: Application to multi-component spinodal decomposition and optimal space tiling*, J. Comput. Phys. **304**, 441–464 (2016).

[52] G. Tegze, G. Bansel, G.I. Tóth, T. Pusztai, Z. Fan and L. Gránásy, *Advanced operator splitting-based semi-implicit spectral method to solve the binary phase-field crystal equations with variable coefficients*, J. Comput. Phys. **228**, 1612–1623 (2009).

[53] X. Wang, L. Ju and Q. Du, *Efficient and stable exponential time differencing Runge-Kutta methods for phase field elastic bending energy models*, J. Comput. Phys. **316**, 21–38 (2016).

[54] S. Wu and J. Xu, *Multiphase Allen-Cahn and Cahn-Hilliard models and their discretizations with the effect of pairwise surface tensions*, J. Comput. Phys. **343**, 10–32 (2017).

[55] Y. Wu, M. Li, Q. Zhang and Y. Liu, *A retinex modulated piecewise constant variational model for image segmentation and bias correction*, Appl. Math. Model. **54**, 697–709 (2018).

[56] M. Xu, H. Guo and Q. Zou, *Hessian recovery based finite element methods for the Cahn-Hilliard equation*, J. Comput. Phys. **386**, 524–540 (2019).

[57] S.-D. Yang, H.G. Lee and J. Kim, *A phase-field approach for minimizing the area of triply periodic surfaces with volume constraint*, Comput. Phys. Commun. **181**, 1037–1046 (2010).

[58] X. Yang, *Efficient linear, stabilized, second-order time marching schemes for an anisotropic phase field dendritic crystal growth model*, Comput. Methods Appl. Mech. Eng. **347**, 316–339 (2019).

[59] X. Yang and L. Ju, *Linear and unconditionally energy stable schemes for the binary fluid-surfactant phase field model*, Comput. Methods Appl. Mech. Eng. **318**, 1005–1029 (2017).

[60] X. Yang, J. Zhao and X. He, *Linear, second order and unconditionally energy stable schemes for the viscous Cahn-Hilliard equation with hyperbolic relaxation using the invariant energy quadratization method*, J. Comput. Appl. Math. **343**, 80–97 (2018).

[61] K. Zhang, W.-S. Hu and Q.-X. Liu, *Quantitatively inferring three mechanisms from the spatiotemporal patterns*, Mathematics **8**, 112 (2020).

[62] Z. Zhang and Z. Qiao, *An adaptive time-stepping strategy for the Cahn-Hilliard equation*, Commun. Comput. Phys. **11**, 1261–1278 (2012).